The Astrophysical Journal, 786:141 (8pp), 2014 May 10 doi:10.1088/0004-637X/786/2/141

EXPECTATIONS FOR THE HARD X-RAY CONTINUUM AND GAMMA-RAY LINE FLUXES FROM THE TYPE IA SUPERNOVA SN 2014J IN M82

Lih-Sin The[1] and Adam Burrows[2]
[1] Department of Physics and Astronomy, Clemson University, SC 29634, USA; tlihsin@clemson.edu
[2] Department of Astrophysical Sciences, Princeton University, Princeton, NJ 08544, USA; burrows@astro.princeton.edu
Received 2014 February 18; accepted 2014 March 31; published 2014 April 25

ABSTRACT

The hard X-ray continuum and gamma-ray lines from a Type Ia supernova dominate its integrated photon emissions and can provide unique diagnostics of the mass of the ejecta, the ^{56}Ni yield and spatial distribution, its kinetic energy and expansion speed, and the mechanism of explosion. Such signatures and their time behavior "X-ray" the bulk debris field in direct fashion, and do not depend on the ofttimes problematic and elaborate UV, optical, and near-infrared spectroscopy and radiative transfer that have informed the study of these events for decades. However, to date no hard photons have ever been detected from a Type Ia supernova in explosion. With the advent of the supernova SN 2014J in M82, at a distance of ∼3.5 Mpc, this situation may soon change. Both *NuSTAR* and *INTEGRAL* have the potential to detect SN 2014J, and, if spectra and light curves can be measured, would usefully constrain the various explosion models published during the last ∼30 yr. In support of these observational campaigns, we provide predictions for the hard X-ray continuum and gamma-line emissions for 15 Type Ia explosion models gleaned from the literature. The model set, containing as it does deflagration, delayed detonation, merger detonation, pulsational delayed detonation, and sub-Chandrasekhar helium detonation models, collectively spans a wide range of properties, and hence signatures. We provide a brief discussion of various diagnostics (with examples), but importantly make the spectral and line results available electronically to aid in the interpretation of the anticipated data.

Key words: gamma rays: stars – radiation mechanisms: non-thermal – radiative transfer – supernovae: general – supernovae: individual (SN 2014J) – X-rays: individual (SN 2014J)

Online-only material: color figures

1. INTRODUCTION

A Type Ia supernova explosion is best modeled as a thermonuclear explosion (of carbon and oxygen, and perhaps some helium) of a degenerate object near one solar mass ($M_\odot$), with a kinetic energy near 10^{51} erg and the production of ∼0.5–∼1.0 $M_\odot$ of radioactive ^{56}Ni (Pankey 1962; Colgate & McKee 1969; Clayton et al. 1969). The object could be a Chandrasekhar white dwarf, the merger product of two white dwarfs (Khokhlov et al. 1993; Höflich et al. 1996), or a slightly sub-Chandrasekhar white dwarf. The explosions could be subsonic deflagrations (Nomoto et al. 1984), sub-Chandrasekhar detonations (Höflich et al. 1996), delayed detonations (Woosley & Weaver 1991; Yamaoka et al. 1992; Höflich 1995; Höflich et al. 1998b), or pulsating delayed detonations (Höflich et al. 1995, 1996) and could start in the deep interior, from distributed hot spots, or near the surface. The product is rich not only in radioactive ^{56}Ni, but in intermediate-mass elements (such as Si, S, Ca, or Ar) and in non-radioactive iron-group isotopes.

Whatever the detailed mechanism and early (first ∼1 s) explosive history, Type Ia supernovae have been studied for decades in the optical, ultraviolet, and near-infrared. Various systematics (such as the "Phillips" relation; Phillips 1993) have been uncovered and profitably used (Riess et al. 1998; Perlmutter 1999), a range of peak brightnesses, atomic abundances, and ^{56}Ni yields have been inferred, and many detailed models of the explosion itself have been proffered. However, though a large fraction of the luminous energy of a Type Ia emerges in a hard X-ray continuum and gamma-ray lines, no Type Ia supernova has yet been observed and scrutinized at these energies. While the optical spectra and light curves require non-local-thermodynamic-equilibrium and time-dependent radiative transfer of thousands of observed energy levels, depending collectively on hundreds of thousands to millions of atomic transitions for scores of ionization states (see, e.g., Pauldrach et al. 2014), the gamma-ray signatures of Type Ia models are relatively simple to generate and understand. The energies and branching ratios of the finite forest of gamma-ray lines produced in the ^{56}Ni(τ = 8.8 days)→^{56}Co(τ = 111.3 days)→^{56}Fe decay sequence are well understood, as are the mean lifetimes (τ) and the positron production factors. The cross sections needed for transfer calculations of the gamma-ray lines are simply those of (inelastic) Compton scattering, photoelectric absorption, and (below ∼70 keV) bremsstrahlung of the secondary electrons. All models early in their expansion become homologous, freezing their density and abundance distributions. Therefore, the gamma-ray lines and hard-photon continuum fluxes as a function of time are ideal signatures of the geometry, abundances, abundance distributions, kinetic energies, and masses of the explosion. In a very real sense, they "X-ray" the debris, and provide the most direct fundamental constraints on Type Ia models.

Recently, a Type Ia supernova, now designated SN 2014J, exploded in the galaxy Messier 82 at a distance of ∼3.5 megaparsecs (Zheng et al. 2014; Goobar et al. 2014; Cao et al. 2014; Kuulkers et al. 2014). Previous theory (e.g., Diehl & Timmes 1998; Ambwani & Sutherland 1988; Burrows 1990; Burrows & The 1990; Burrows et al. 1991; Bussard et al. 1989; Chan & Lingenfelter 1991; Höflich et al. 1998a; Maeda et al. 2012; Milne et al. 2004; Summa et al. 2013) indicates that at such a close distance its gamma-ray lines with energies of 812, 847, and 1238 keV might be detectable by *INTEGRAL*/Space Platform Interferometry (SPI; Roques et al. 2003; Vedrenne et al.

2003). For a 10^6 s integration, *INTEGRAL*/SPI has an approximate narrow-line 3σ sensitivity at 1 MeV of 3.1×10^{-5} photons cm^{-2} s^{-1}. It also has a spectral resolution near 1.3 MeV of ~2.5 keV, sufficient in principle to resolve the various gamma-ray lines whose widths have been estimated to be 10–20 keV (Burrows & The 1990; Bussard et al. 1989). Even more, the supernova's hard X-ray Compton continuum from ~30 keV to ~80 keV should easily be observed by *NuSTAR*, boasting a 10^6 s sensitivity of a few $\times 10^{-8}$ photons cm^{-2} s^{-1} keV^{-1} in this energy range (Harrison et al. 2013; Koglin et al. 2005). The hard continuum of SN 2014J might also be observed by *INTEGRAL*/IBIS/ISGRI (Lebrun et al. 2003), with a 3σ sensitivity from ~20 to ~100 keV of a few $\times 10^{-6}$ photons cm^{-2} s^{-1} keV^{-1}[3]. Excitingly, and by the end of 2014, ASTRO-H will be launched and will have capabilities in the region below 100 keV comparable to those of *NuSTAR*. Specifically, below ~100 keV, HXI on ASTRO-H will have a 3σ sensitivity for a 10^6 s integration of a few $\times 10^{-8}$ photons cm^{-2} s^{-1} keV^{-1} (Kokubun et al. 2010). SGD on ASTRO-H has a design sensitivity over the 100–450 keV range of $5–10 \times 10^{-8}$ photons cm^{-2} s^{-1} keV^{-1} for a 10^6 s integration (Tajima et al. 2010).

There already exist in the literature many predictions for the hard photon signatures of many disparate Type Ia models (see above). The gamma-ray line light curves, line shapes, hard X-ray continuum flux spectrum, flux band ratios, and the ratio of the hard X-ray fluxes to those of the gamma-ray lines are together sensitive to and diagnostic of the ^{56}Ni yields, ^{56}Ni and high-Z element spatial distributions and mixing, total masses, explosion kinetic energies, explosion asymmetries, and the distinction between supersonic detonation and subsonic deflagration (for a review, see Burrows 1990). Depending on model, the peak gamma-line flux occurs ~60–90 days after explosion, the Comptonization continuum from ~30 keV to ~1 MeV peaks earlier (near day 20–30), and is usefully diagnostic of model before day 60, and the spectral peak of the continuum is found near ~100–200 keV before day 100. The fluxes below ~100 keV are very sensitive to photoelectric absorption in the debris, which in turn is related to iron-peak yield and its spatial distribution. If there are iron-peak isotopes near the debris surface, the fluxes below ~100 keV can be severely photoelectrically suppressed, while the corresponding gamma-ray lines fluxes near ~1 MeV are higher. The Compton continuum flux above ~100 keV would also be higher. Hence, the ratios of the hard X-ray flux below ~100 keV to the continuum flux above ~100 keV or to the gamma line fluxes near ~1 MeV are strongly dependent on the iron-peak distribution. Correspondingly, if the ^{56}Ni is more deeply buried in the debris, the hard X-ray fluxes below ~100 keV are enhanced and these systematics are reversed. Moreover, if the explosion energies are large, and/or the ^{56}Ni yields high, the ^{56}Co-decay line fluxes at 847 and 1238 keV can be 50%–100% higher. The line shapes directly reflect the distribution of the produced ^{56}Ni in velocity space (Burrows & The 1990). In fact, an analytic model for these line shapes, including Doppler shift effects and distinguishing the matter and ^{56}Ni distributions, has been developed (Bussard et al. 1989).

We surmise, however, that a focused set of new calculations in aid of the ongoing SN 2014J campaign to detect its hard continuum and line emissions might be of use. In this spirit, we calculate in this paper various theoretical hard-photon signatures for a representative set of Type Ia explosion models, put at the 3.5 megaparsec distance of M82. The results can be scaled to any other distance using the inverse square law. The model results are also provided in tabular form (at http://www.astro.princeton.edu/~burrows/sn2014j/) to help observers engaged in measurement and interpretation efforts navigate the theoretical terrain. In this paper, we don't provide gamma-ray line profiles, but encourage the interested reader to explore the associated predictions of Burrows & The (1990) and the analytic model of Bussard et al. (1989).

2. METHOD

To derive the emergent spectrum at a given post-explosion time, we employ the variance reduction Monte Carlo code developed in Burrows & The (1990) and The et al. (1990), augmented to include the bremsstrahlung X-ray production of the Compton electrons and the iron fluorescence line at ~6.4 keV (Clayton & The 1991; The et al. 1994). The 6 most prominent lines of ^{56}Ni decay (including the 158, 750, and 812 keV lines) and the 45 most prominent lines of ^{56}Co decay (the most important of which are at 847, 1238, 1772, and 2598 keV) are followed from emission, through Compton scatterings, to either photoelectric absorption in the homologously expanding debris or escape.[4] The production of positrons is included, but they are assumed to form positronium instantaneously and to annihilate in situ (Bussard et al. 1979). Both two-photon (25%) and three-photon (75%) decays are allowed, and those photons are then followed in the Monte Carlo. The electron–positron pair-production cross section is taken from Ambwani & Sutherland (1988), the full angle-dependent Klein–Nishina formula for Compton scattering is used, and the photoelectric cross sections for the 31 most abundant elements thought to reside in Type Ia debris are taken from Veigele (1973) and Henke et al. (1982). Since the matter speeds are small compared with the speed of light, we do not include Doppler shifts due to matter motions (thermal or bulk) in the calculations. These would need to be included if we were to focus on the detailed line profiles, but for the integrated line emissions they are not germane.

The bremsstrahlung calculation proceeds as follows: for each gamma-ray photon from the decays of ^{56}Ni and ^{56}Co that Compton scatters, its new direction and energy are calculated by Monte Carlo sampling using the Klein–Nishina differential cross section. At the same time, the recoil kinetic energy of the electron and its location are recorded for post-processing. When post-processing to derive the bremsstrahlung flux, we assume the energetic electrons slow down by inelastic collisions with atoms and plasma ions where they were Comptonized. For each recorded Comptonized electron, we calculate the bremsstrahlung spectrum generated in the medium (see Clayton & The 1991). Then, we follow the propagation of the bremsstrahlung photons using the same Monte Carlo procedure

[3] *INTEGRAL*/IBIS also has capabilities from ~15 keV to ~1 MeV, with the potential for detections at the ~few $\times 10^{-5}$ cm^{-2} s^{-1} keV^{-1} level between ~100 and 1000 keV (Isern et al. 2013). The *Suzaku* HXD detector (Takahashi et al. 2007) extends to ~200 keV (and with reduced effective area to ~600 keV) and might have a shot at detecting this supernova at early times (perhaps near ~20 days after explosion) and at the higher continuum energies.

[4] We also include the 10 lines of ^{57}Co decay, for which the 14.4, 122, and 136 keV lines are the most important. For model W7, the mass of ^{57}Ni is $4.81 \times 10^{-2}\ M_\odot$. For models W7E and W7A, the mass of ^{57}Ni is $8.5 \times 10^{-3}\ M_\odot$. For model w7dn, the mass of ^{57}Ni is $2.60 \times 10^{-2}\ M_\odot$ and for model w7dt it is $2.72 \times 10^{-2}\ M_\odot$. For all other models, we assume a solar ratio for ^{57}Ni/^{56}Ni of (1/41). At these levels, the continuum results before day 100 are very little affected.

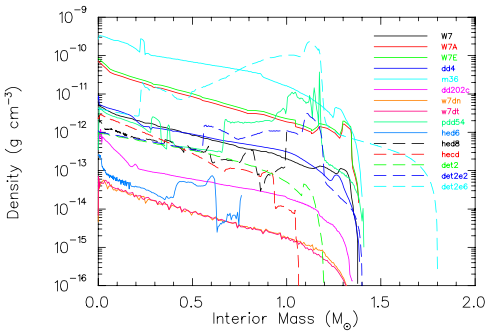

Figure 1. Density (in g cm^{-3}) vs. interior mass (in $M_\odot$) at day 10 for the 15 models studied in this paper. For clarity of presentation, W7A is multiplied by 10, W7E is multiplied by 12, m36 is multiplied by 100, w7dn and w7dt are divided by 100, and hed6 is divided by 10. Note that the expansion is homologous and that the density at a given interior mass scales as $(1/t^3)$, where t is the time since the start of explosion.

(A color version of this figure is available in the online journal.)

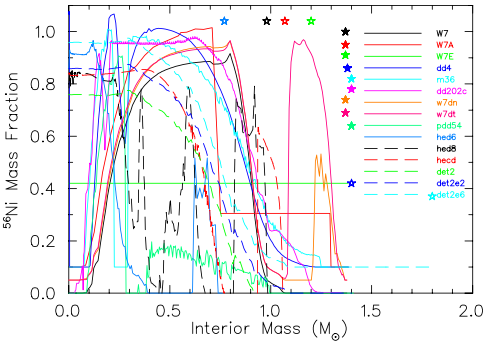

Figure 2. ^{56}Ni fraction vs. interior mass (in $M_\odot$) for the 15 models highlighted in this paper. This figure depicts the ^{56}Ni distribution for each model. To attempt a degree of clarity in what would otherwise be even more of a jumble, we have shifted the fractions for W7A by −0.1, dd4 by +0.1, m36 by +0.1, w7dn by +0.05, w7dt by +0.05, hed8 by −0.1, hecd by −0.1, det2 by −0.1, and det2e6 by + 0.1. Note that the various models have different total ejecta masses, a fact reflected by the different positions of the star symbols with the associated model colors that identify the outer boundary mass of a given model. See Table 1.

(A color version of this figure is available in the online journal.)

used for the gamma-ray lines. Photoelectric absorption, electron collisions, and electron-capture on ^{56}Fe parent's nuclei create shell vacancies in ions. Each K-shell vacancy is followed by K X-ray fluorescence and the number of K X-ray line photons generated is calculated by multiplying the number of K-shell vacancies by the K-shell fluorescence yield of the absorbing atoms (Bambyneck et al. 1972). The number of K X-ray line photons that emerges is then calculated by the self-same Monte Carlo method. The et al. (1994) estimate that most of the 6.4 keV Fe K-shell X-ray production is due in fact to the electron-capture process, so that since we do not include ionization due to electron collisions our calculated Fe K X-ray line fluxes are probably accurate to ∼10%.

All the explosion models we study are spherical, though we have observed that the differences in gamma-ray signatures between aspherical (e.g., Summa et al. 2013; Maeda et al. 2012) and spherical models are not as large as the differences between the vast array of published spherical models, with their disparate ^{56}Ni yields and distributions, heavy-element distributions, kinetic energies, and burning regimes. We use the element and density distributions provided by the original Type Ia model builders (except in the few cases when we have artificially mixed the ejecta), and have endeavored in choosing the subset of models we highlight here to cover as wide a range of anticipated behaviors as possible.

Therefore, for this SN 2014J study we have chosen 15 models in the literature to represent the range of Type Ia explosion models. They span the model space discussed over the last 30 years, though are all spherical realizations, and include deflagrations (W7; Nomoto et al. (1984), along with mixed variants W7E and W7A), delayed detonations (dd4—Woosley & Weaver 1991; w7dn, w7dt—Yamaoka et al. 1992; m36—Höflich 1995; dd202c—Höflich et al. 1998b), pulsating delayed detonations (pdd54—Höflich et al. 1995), merger detonations (det2, det2e2, det2e6—Khokhlov et al. 1993; Höflich et al. 1996), and sub-Chandrasekhar helium detonations (hed6, hed8, hecd—Höflich et al. 1996).

W7 is a fiducial Chandrasekhar deflagration model with an explosion energy of 1.3×10^{51} erg and a ^{56}Ni mass of 0.58 $M_\odot$ that seems to fit well the spectra and light curves of normal Type Ias. Model W7E fully mixes the ^{56}Ni, and model W7A partially mixes it. dd4 is a delayed detonation with an explosion energy of 1.24×10^{51} erg, a total mass of 1.39 $M_\odot$, and a ^{56}Ni mass of 0.61 $M_\odot$. w7dn is a delayed detonation model of 1.37 $M_\odot$ with an explosion energy of 1.6×10^{51} erg, constructed to have the same core distribution of ^{56}Ni as W7, but given an extra ^{56}Ni surface cap of 0.04 $M_\odot$. Hence, model w7dn has a total ^{56}Ni mass of 0.62 $M_\odot$. w7dt is the same as w7dn, but with an explosion energy of 1.61×10^{51} erg and an extra outer layer of 0.18 $M_\odot$ of ^{56}Ni, for a total ^{56}Ni mass of 0.76 $M_\odot$. m36 is a delayed detonation model with an explosion energy of 1.51×10^{51} erg and 0.59 $M_\odot$ of ^{56}Ni. dd202c is a delayed detonation model with an explosion energy of 1.27×10^{51} erg and a continuous ^{56}Ni distribution from the core to an interior mass point of 1.2 $M_\odot$, with a total mass of 1.40 $M_\odot$ and a ^{56}Ni mass of 0.72 $M_\odot$. pdd54 is pulsating delayed detonation model with an explosion energy of 1.02×10^{51} erg, in which slow deflagration leads to burning inefficient enough to induce pulsation before detonation. This model has a total ^{56}Ni mass of 0.17 $M_\odot$. det2 is a merger detonation model having an explosion energy of 1.54×10^{51} erg, a total mass of 1.20 $M_\odot$, and a ^{56}Ni mass of 0.62 $M_\odot$. det2e2 is a merger detonation model with an explosion energy of 1.44×10^{51} erg, a total mass of 1.40 $M_\odot$, and a ^{56}Ni mass of 0.63 $M_\odot$. det2e6 is a merger detonation model with an explosion energy of 1.43×10^{51} erg, a total mass of 1.80 $M_\odot$, and a ^{56}Ni mass of 0.63 $M_\odot$. hed6 is a He-detonation model with an explosion energy of 0.72×10^{51} erg, a total mass of 0.77 $M_\odot$, and a ^{56}Ni mass of 0.26 $M_\odot$. hed8 is a He-detonation model with an explosion energy of 1.03×10^{51} erg, a total mass of 0.96 $M_\odot$, and a ^{56}Ni mass of 0.51 $M_\odot$. Finally, hecd is a superluminous helium-detonation model with an explosion energy of 1.3×10^{51} erg, a total mass of 1.07 $M_\odot$, and a ^{56}Ni mass of 0.72 $M_\odot$. These last three sub-Chandrasekhar detonation models (hed6, hed8, and hecd) all have central ^{56}Ni concentrations, as well as outer surface layers of ^{56}Ni. All together, these 15 models span the model space rather well. We plot the 15 model density profiles in Figure 1 (at day 10) and their ^{56}Ni distributions in Figure 2. Figure 1 demonstrates the wide range in density profiles represented, from the high densities of model det2e6 to the much lower densities of model hed6. Note the enhancements in the outer densities of models det2e2 and pdd54. Table 1 summarizes the basic model specifications.

A few approximate facts are worth noting. The peak gamma line fluxes occur near a time, $t_p \propto (\kappa_\gamma (M^2 \tau / E))^{1/3}$, with a peak flux $F_p \propto (1/\tau) e^{-(3t_p/2\tau)}$, where M is the debris mass, E is the

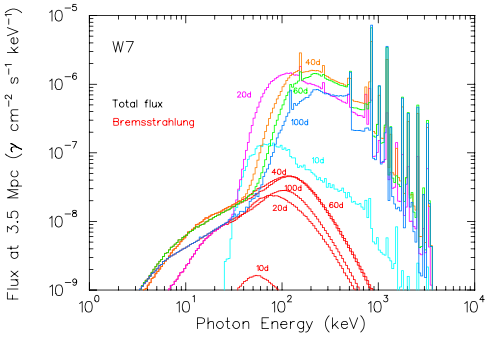

Figure 3. Flux spectra at a distance of 3.5 Mpc in photons cm^{-2} s^{-1} keV^{-1} for the emergent hard X-ray photons and gamma-ray lines 10, 20, 40, 60, and 100 days after explosion for the fiducial model W7. The photon energy is in keV from 1 keV to ∼3.2 MeV. Included are curves for the total flux and its bremsstrahlung contribution, indicating the importance of bremsstrahlung below ∼60 keV. Note that the line fluxes depicted are per plotting bin width, and are not resolved. They show the line positions, but the relative heights are only crude measures of the actual fluxes, whose integrals (the total line fluxes) are shown correctly in photons cm^{-2} s^{-1} in Figures 14–16.

(A color version of this figure is available in the online journal.)

Table 1
Type Ia Explosion Model Characteristics

Model	Total Mass ($M_\odot$))	^{56}Ni Mass ($M_\odot$)	Explosion Energy (10^{51} erg)	Reference
W7	1.38	0.58	1.3	1
W7E	1.38	0.58	1.3	1
W7A	1.38	0.58	1.3	1
dd4	1.39	0.61	1.24	2
w7dn	1.37	0.62	1.6	3
w7dt	1.37	0.76	1.61	3
m36	1.39	0.59	1.51	4
dd202c	1.4	0.72	1.27	5
pdd54	1.38	0.17	1.02	6
det2	1.2	0.62	1.54	7
det2e2	1.4	0.63	1.44	7
det2e6	1.8	0.63	1.43	7
hed6	0.77	0.26	0.72	7
hed8	0.96	0.51	1.03	7
hecd	1.07	0.72	1.3	7

References. (1) Nomoto et al. (1984); (2) Woosley & Weaver (1991); (3) Yamaoka et al. (1992); (4) Höflich (1995); (5) Höflich et al. (1998b); (6) Höflich et al. (1995); (7) Höflich et al. (1996).

explosion kinetic energy, τ is the mean life of the decay, and κ_γ is the Compton opacity of the line. Bussard et al. (1989) have demonstrated that this behavior generally tracks the calculated numerical behavior rather well. The approximate number of Compton scatterings of an ∼MeV gamma ray necessary to downscatter to a photon energy of ε_γ is $\sim(m_e c^2/\varepsilon_\gamma)$. So, to achieve $\varepsilon_\gamma = 50$ keV requires ∼10 scatterings. The Compton cross sections at 847, 1238, and 3200 keV are $0.344\sigma_T$, $0.285\sigma_T$, and $0.166\sigma_T$, respectively, where σ_T is the Thomson cross section. After ∼150 days, much of the continuum flux below $m_e c^2 = 511$ keV is due to the three-photon decay of positronium, and below the 122 and 136 keV lines of ^{57}Co due to their Comptonization (if ^{57}Ni is present).

3. RESULTS

Rather than plot all the results for all 15 models, we highlight a few representative models with which to demonstrate various common effects. Figures 3–6 depict the flux spectra of the

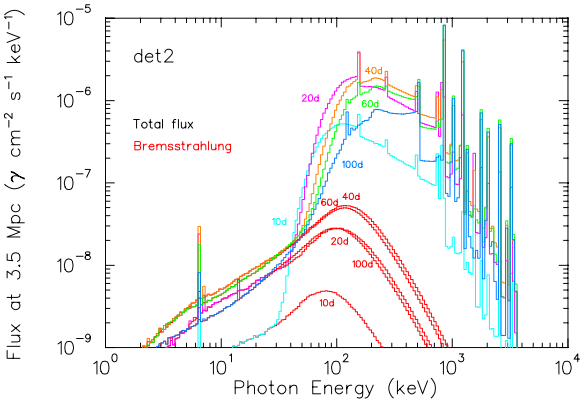

Figure 4. Same as Figure 3, but for model det2. Note that the continuum and line fluxes for this detonation model at the early phases (e.g., 10 days) are much higher at higher photon energies, and lower at lower photon energies. The former is due to the more rapid expansion, that liberates the hardest photons more quickly, while the latter is due to greater photoelectric absorption by the enhanced ^{56}Ni mass and the presence of iron-peak elements near the periphery. The presence of iron-peak nuclei in the outer regions results in a visible iron fluorescence line at ∼6.4 keV, absorbed in W7 (Figure 3).

(A color version of this figure is available in the online journal.)

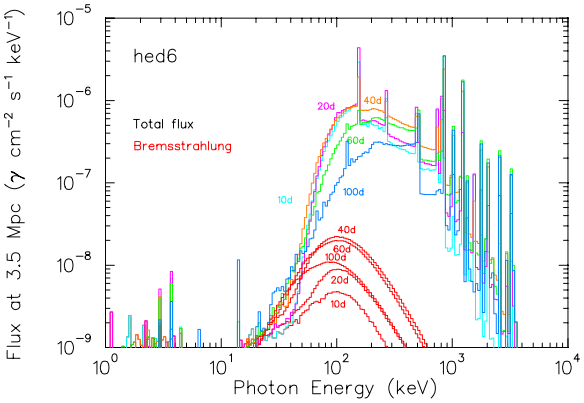

Figure 5. Same as Figure 3, but for detonation model hed6. Note that the band fluxes below ∼50 keV are even more suppressed than those for model det2 (Figure 4). This is due to photoelectric absorption by the ^{56}Ni cap at the very periphery of this model. Note also that concommitantly for this model the hard X-ray continuum above ∼60 keV and the gamma-line fluxes are significantly higher at day 10, but lower at day 100. The former reflects, among other things, the lower total mass of hed6, while the latter reflects the higher ^{56}Ni yield of model det2.

(A color version of this figure is available in the online journal.)

emergent hard X-ray photons and gamma-ray lines at various epochs after explosion from 10 to 100 days for representative deflagration (W7), merger detonation (det2), helium detonation (hed6), and pulsating delayed detonation (pdd54) models. Note that the continuum fluxes for many models peak near ∼200 keV and day 40 (except for the pdd54 model), but that the deviations from this behavior are discriminating. The calculations include the bremsstrahlung contributions of the Compton secondaries. For all models, the continuum flux peak slides to higher energies with time, while the spectral slope between ∼40 and ∼100 keV (always positive) decreases. The (mostly) bremsstrahlung fluxes below ∼30 keV have positive slope near ∼1.0. As these figures suggest, if the iron-peak elements do not reside in the outer zones of the debris in abundance (as they do, for instance, for models hed6, w7dn, and w7dt), bremsstrahlung below ∼60 keV can be quite important. This will be particularly relevant to the interpretation of anticipated *NuSTAR* data. The continuum and

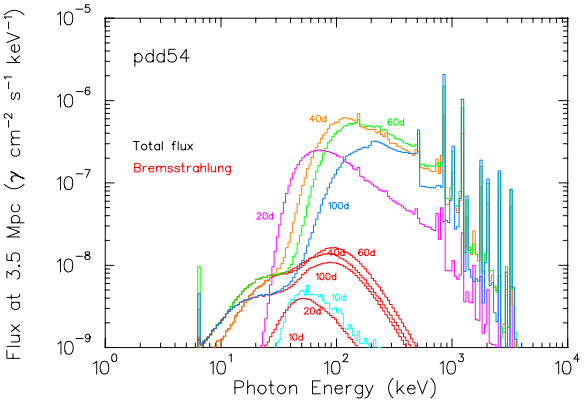

Figure 6. Same as Figure 3, but for pulsating delayed detonation model pdd54. The low flux values are reflective mostly of the low ^{56}Ni burden in this model. Note that the flux for this model at day 20 is approximately three times lower at ∼70 keV than the corresponding flux for model W7, and that the photon energy at peak has also shifted to lower energies.

(A color version of this figure is available in the online journal.)

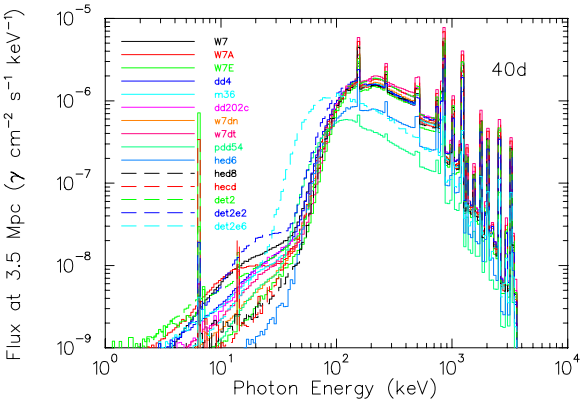

Figure 7. Same as Figure 3, but for all 15 models at day 40. The model-to-model variation of fluxes at this epoch (as well as at others) is quite wide throughout the spectral interval depicted, but is particularly interesting in the *NuSTAR* bands. For completeness, we also include the 6.4 keV fluorescence line of iron.

(A color version of this figure is available in the online journal.)

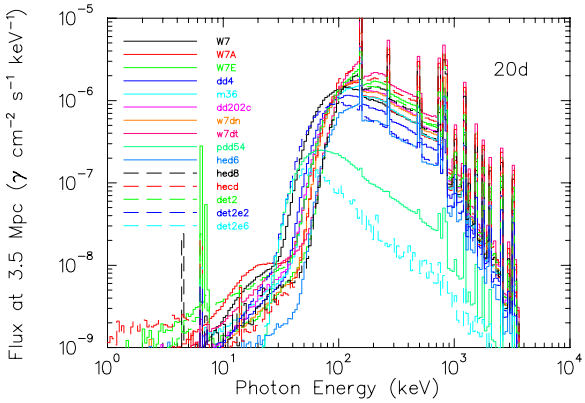

Figure 8. Same as Figure 7, but for all 15 models at day 20. This figure clearly demonstrates the diagnostic differences between the various models at all energies.

(A color version of this figure is available in the online journal.)

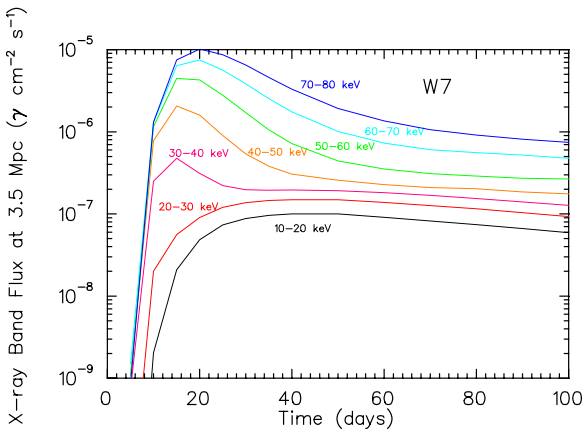

Figure 9. Light curves of hard X-rays in 10 keV width bins for the representative deflagration model W7. The curves include bremsstrahlung by Compton electrons. Note that the curves peak early during the Type Ia supernova development, near day 20, that the hardest bands are generally the brightest (below ∼100 keV), and that the curves decay rather slowly after peak.

(A color version of this figure is available in the online journal.)

line fluxes for merger detonation model det2 are higher earlier than for model W7, particularly earlier than day 10, but are similar to those for model W7 at later times, while W7's peak fluxes for the hard X-rays below 100 keV are higher than those for model det2.

For model hed6, the fluxes below ∼40 keV are suppressed with respect to those for models W7 and det2. This is due to photoelectric absorption by the ^{56}Ni cap at the periphery of model hed6 and to its smaller ejecta mass. Interestingly, at day 10 and earlier, the fluxes at energies above 50 keV for model hed6 are higher than those for model W7, while later than day 60 its line and continuum fluxes are lower than those for model W7 (reflecting hed6's lower ^{56}Ni mass). The generally low flux values for the pulsating delayed detonation model pdd54 shown in Figure 6 reflect the low ^{56}Ni yield in this model. Note that the flux at ∼70 keV for this model at day 20 is approximately three times lower than the corresponding flux for model W7, but that near ∼30 keV the fluxes for these two models are comparable. The slow expansion speed of model pdd54 and high cap densities leave the densities higher longer and scatters more photons at these times to lower energies, but the lower ^{56}Ni yield partially compensates. The photon energy at peak near day 40 has also shifted from the ∼200 keV for many models to ∼100 keV for model pdd54, and this model has ∼20% to a factor of ∼3× lower flux.

Figures 7 and 8 compare the spectra at days 40 and 20 for all 15 models investigated, summarizing some of the clear spectral differences between them. We call attention to the high fluxes for model det2e6 below ∼100 keV at day 40, caused by its relatively dense ejecta (an efficient converter of MeV lines to X-ray continuum by Compton scattering), but also the low fluxes above ∼40 keV for this same model at day 20. As Figure 7 demonstrates, at day 40 the continuum fluxes below ∼40 keV and above ∼200 keV and the line fluxes in the MeV range distinguish the various models most clearly. However, as Figure 8 demonstrates, the continuum and line fluxes in all energy ranges at earlier times (such as day 20) are even more discriminating.

Figures 9–12 portray the light curves of hard X-rays in 10 keV width bins for the representative models W7, det2, hed6, and pdd54. These plots are particularly relevant to *NuSTAR*. Bremsstrahlung is important below ∼60 keV, particularly at later times. Note that the curves peak (depending on the energy bin) early during a Type Ia supernova. For model W7, they peak near day 20; for model det2 they peak between days 10 to 30 (depending on energy bin); for model hed6, there is an

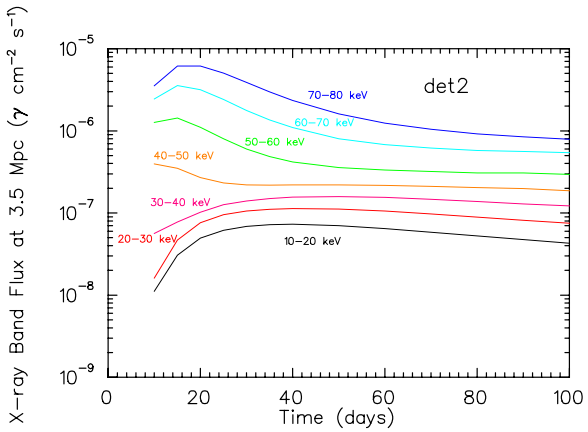

Figure 10. Same as Figure 9, but for detonation model det2. Note that these band fluxes are suppressed at later times relative to those for model W7 (Figure 9) by the enhanced photoelectric absorption in model det2. However, due to the rapid expansion, all the band fluxes for det2 are higher than in fiducial model W7 at the earliest epochs after explosion. This is one diagnostic signature of the rapid disassembly of detonations, as opposed to deflagrations, and the proximity of ^{56}Ni to the periphery in the former.

(A color version of this figure is available in the online journal.)

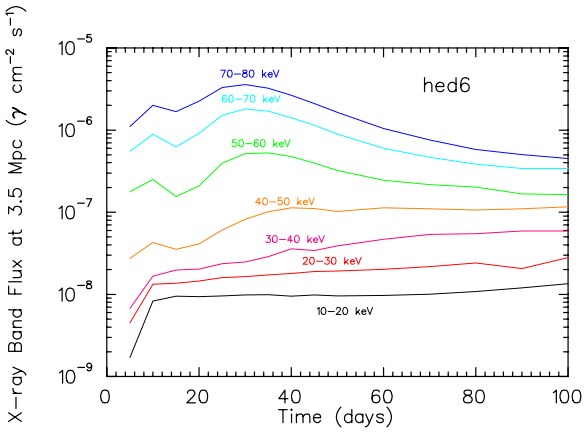

Figure 11. Same as Figure 9, but for detonation model hed6.

(A color version of this figure is available in the online journal.)

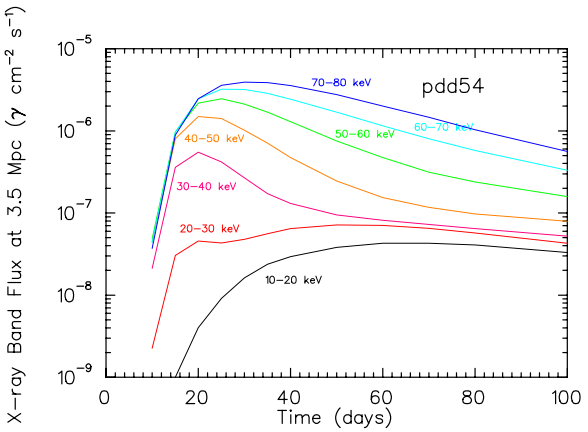

Figure 12. Same as Figure 9, but for pulsating delayed detonation model pdd54.

(A color version of this figure is available in the online journal.)

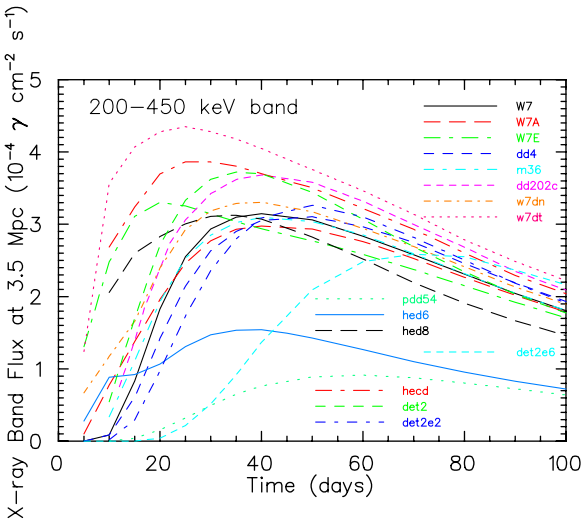

Figure 13. Light curves in the 200–450 keV band for all 15 models studied in this paper. Note the diagnostic differences in the evolution of this band flux. It is expected that the SGD detector on ASTRO-H will be sensitive to many Type Ia models in this band out to distances slightly greater than ∼10 Mpc.

(A color version of this figure is available in the online journal.)

early, weaker peak, followed by a brighter peak from 50 to 80 keV near day 30; and model pdd54 peaks between days 20 and 30. The hardest bands below ∼100 keV are generally the brightest, and the curves decay rather slowly after peak. In fact, these band fluxes are roughly constant from day 60 to after day 100 for models W7, det2, and hed6—less so for model pdd54. For model det2, due to its rapid expansion and more outward distribution of ^{56}Ni, the band fluxes for det2 peak earlier than in model W7. This is one diagnostic of the rapid disassembly of detonations, as opposed to deflagrations, and the proximity of ^{56}Ni to the periphery in the former. However, above 30 keV and at later times the band fluxes of models det2 and W7 are comparable. As Figure 11 indicates (and as noted earlier), the hard X-ray band fluxes for helium detonation model hed6 are much higher than those for model W7 before day 10, though thereafter those for model W7 quickly exceed those for model hed6. Note that the early fluxes for model pdd54 are quite different from those for model hed6, but that near day 40 they are comparable in the 70–80 keV band. These examples (among others) emphasize that a time series (in addition to a spectrum) is important to properly discriminate between the very different models. Though not accessible to *NuSTAR*, in anticipation of the launch of ASTRO-H, with its SGD detector with sensitivity in the 200–450 keV range, we provide in Figure 13 light curves in this broad band for all 15 models. As noted earlier, the fluxes in this region of the spectrum can be quite diagnostic of model.

Figures 14 and 15 plot the light curves (in days after explosion) of the 847 and 1238 keV lines of ^{56}Co decay at a distance of 3.5 Mpc for the entire suite of 15 models with which we have chosen to depict the wide range of Type Ia explosion models in the literature. These curves are most germane to *INTEGRAL* and its SN 2014J campaign. The peak emission occurs for most models approximately between day 60 and day 100, but the early rise of a light curve is a stiff function of model. For instance, at day 40 these line fluxes vary from model to model by an order of magnitude, and the fluxes at day 20 vary by more than two orders of magnitude. At late times, the 847 and 1238 keV line fluxes reflect the bulk ^{56}Ni yield. In this sense, some of our models overlap with the line predictions of Maeda et al. (2012). Note that merger detonation model det2e6, with its larger total mass (1.80 $M_{\odot}$) and "anomalous" mass distribution (Figure 1) has, as a result, quite muted line fluxes during the

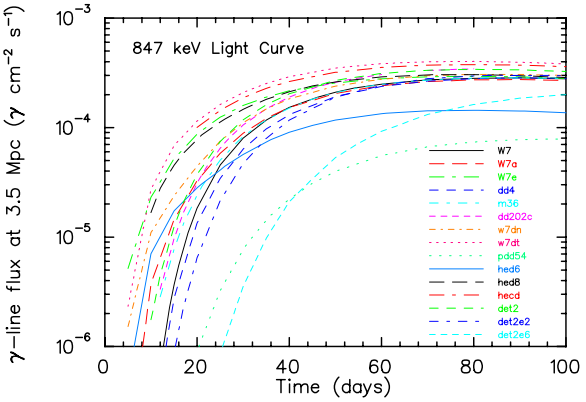

Figure 14. Light curves in photons cm^{-2} s^{-1} vs. time (in days after explosion) of the 847 keV line of ^{56}Co decay at a distance of 3.5 Mpc for 15 Type Ia explosion models in the literature. The peak emission occurs between day 60 and day 100, but the time at which this light curve first exceeds a given threshold is a sharp function of model. The fluxes at day 40, for instance, vary by almost an order of magnitude, and the fluxes at day 20 can vary by a factor of 30.

(A color version of this figure is available in the online journal.)

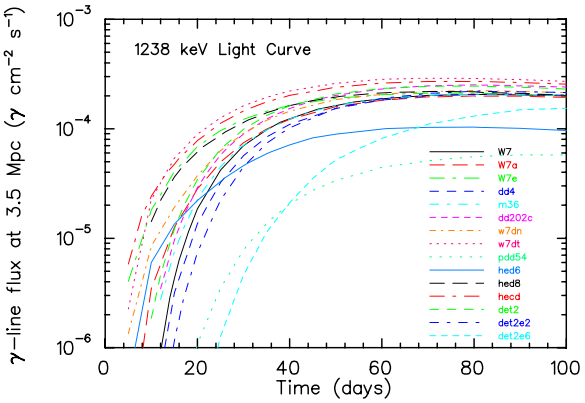

Figure 15. Same as Figure 14, but for the 1238 keV line of ^{56}Co.

(A color version of this figure is available in the online journal.)

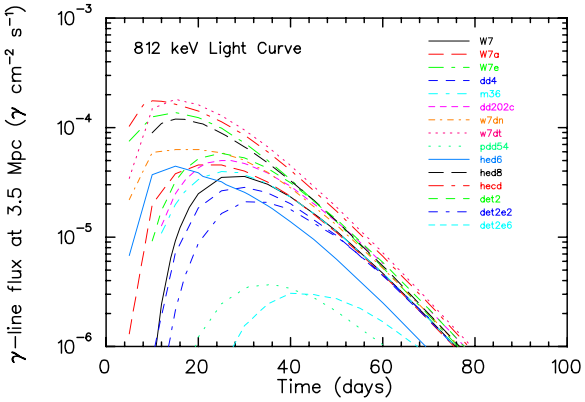

Figure 16. Same as Figure 14, but for the 812 keV line of ^{56}Ni. Note that the peak values can vary by approximately two orders of magnitude, that the peaks occur earlier than those for the 847 and 1238 keV lines, and that they decay much faster. The 812 keV line is one of the most diagnostic of model, but is more difficult to see.

(A color version of this figure is available in the online journal.)

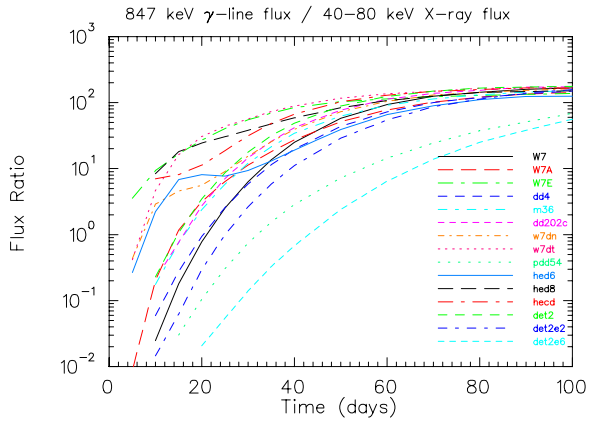

Figure 17. Ratio of the 847 keV line flux to the total flux in a 40–80 keV bin vs. time (in days since explosion), for all 15 models investigated in this study. Such flux ratios are very diagnostic of model, varying as they do at a given epoch after day 20 and from model to model by factors of more than 1000.

(A color version of this figure is available in the online journal.)

first hundred days, but larger Compton continuum fluxes below ∼100 keV.

Figure 16 depicts the corresponding light curve for the 812 keV line of ^{56}Ni. The peak fluxes differ from model to model by approximately a factor of 100 and occur between days 10 and 30. This is much earlier than the corresponding peaks for the 847 and 1238 lines of ^{56}Co (as well as for its other lines), and the 812 keV line flux decays much faster for all models. The early emergence and fast decay of the 812 keV line are mostly due to the shorter decay time of ^{56}Ni ($\tau = 8.8$ days), while the lower fluxes reflect the greater Compton opacities at these earlier (denser) times. Therefore, the strength of this line is an important signature of the rapidity with which the debris expands and becomes transparent to Compton scattering. As a result, it is an important diagnostic of the expansion speed and the total mass of the ejecta, as well as of the presence of ^{56}Ni in the outer zones, and can discriminate well between most detonation and deflagration models. However, the lower associated fluxes make it more difficult to capture.

Figure 17 combines aspects of both the continuum and line signatures of the various models to provide a good metric with which to distinguish them. It depicts the evolution of the ratio of the 847 keV line flux to the total flux in a 40–80 keV bin for all 15 models studied in this paper. Such line−continuum flux ratios (others can easily be envisioned) are very diagnostic of model, varying as they do from model to model by factors of more than 100, depending on epoch. A number of models have high continuum fluxes below ∼100 keV when they also have low line fluxes near ∼1 MeV (as well as low continuum fluxes from ∼100 to 1000 keV), and vice versa. Therefore, such ratios amplify the model differences rather well. Their usefulness does, however, depend on getting good data for both line and continuum. Figure 17 emphasizes that such ratios are most diagnostic at earlier epochs.

4. CONCLUSION

We have calculated the line fluxes from ^{56}Ni and ^{56}Co decay and escape for the dominant lines of this beta decay chain, the concomitant hard X-ray Compton and bremsstrahlung continua, and the iron fluorescence line fluxes for 15 representative Type Ia explosion models. The inclusion of bremsstrahlung (for the first time for most of the 15 models) is particularly important for the proper interpretation of the anticipated *NuSTAR* data. We have done this without preconceived notions of which explosion models or modalities might be preferred from previous

considerations. From the line light curves and ratios, continuum band fluxes and their temporal evolution, and rise times and peak magnitudes, one may hope to constrain the various physical parameters of the explosion, and, perhaps, eliminate classes of explosion models while determining explosion parameters. In principle, the ^{56}Ni yields and distributions, kinetic energies, and total ejecta masses (among other things) can be measured. Our model results are available in electronic form at http://www.astro.princeton.edu/∼burrows/sn2014j/ to aid in the interpretation of the hard photon data anticipated in the ongoing SN 2014J, as well as future, observing campaigns.

A.B. acknowledges association with the Joint Institute for Nuclear Astrophysics (JINA, NSF PHY-0822648), and funding through the NSF PetaApps program, under award OCI-0905046 via subaward No. 44592 from Louisiana State University to Princeton University. We thank P. Hoflich, S. Kumagai, K. Nomoto, P. Pinto, and S. Woosley for access to their supernova models. L.-S.T. thanks P.A. Milne for assistance in compiling the supernova models.

REFERENCES

Ambwani, K., & Sutherland, P. 1988, ApJ, 325, 820
Bambyneck, W., ann, B., Fink, R. W., et al. 1972, RvMP, 44, 716
Burrows, A. 1990, in AIP Conf. Proc. 232, Gamma-Ray Line Astrophysics, ed. P. Durouchoux & N. Prantzos (Melville, NY: AIP), 297
Burrows, A., Shankar, A., & Van Riper, K. A. 1991, ApJL, 379, L7
Burrows, A., & The, L.-S. 1990, ApJ, 360, 626
Bussard, R. W., Burrows, A., & The, L.-S. 1989, ApJ, 341, 401
Bussard, R. W., Ramaty, R., & Drachman, R. 1979, ApJ, 228, 928
Cao, Y., Kasliwal, M. M., McKay, A., & Bradley, A. 2014, ATel, 5786
Chan, K. W., & Lingenfelter, R. E. 1991, ApJ, 368, 515
Clayton, D. D., Colgate, S. A., & Fishman, G. 1969, ApJ, 155, 75
Clayton, D. D., & The, L.-S. 1991, ApJ, 375, 221
Colgate, S. A., & McKee, C. 1969, ApJ, 157, 623
Diehl, R., & Timmes, F. X. 1998, PASP, 110, 637
Goobar, A., Johansson, J., Amanullah, R., et al. 2014, ApJL, 784, L12
Harrison, F. A., Craig, W. W., Christensen, F. E., et al. 2013, ApJ, 770, 103
Henke, B. L., Lee, P., Tanaka, T. J., Shimabukuro, R. L., & Fujikawa, B. K. 1982, ADNDT, 27, 1
Höflich, P. 1995, ApJ, 443, 89
Höflich, P., Khokhlov, A. M., & Wheeler, J. C. 1995, ApJ, 444, 831
Höflich, P., Khokhlov, A., Wheeler, J. C., et al. 1996, ApJL, 472, L81
Höflich, P., Wheeler, J. C., & Khokhlov, A. 1998a, ApJ, 492, 228
Höflich, P., Wheeler, J. C., & Thielemann, F. K. 1998b, ApJ, 495, 617
Isern, J., Jean, P., Bravo, E., et al. 2013, A&A, 552, A97
Khokhlov, A., Mueller, E., & Höflich, P. 1993, A&A, 270, 223
Koglin, J. E., Christensen, F. E., Craig, W. W., et al. 2005, Proc. SPIE, 5900, 266
Kokubun, M., Nakazaka, K., Enoto, T., et al. 2010, Proc. SPIE, 7732, 515
Kuulkers, E., et al. 2014, ATel, 5835
Lebrun, F., Leray, J. P., Lavocat, P., et al. 2003, A&A, 411, L141
Maeda, K., Terada, Y., Kasen, D., et al. 2012, ApJ, 760, 54
Milne, P. A., Hungerford, A. L., Fryer, C. L., et al. 2004, ApJ, 613, 1101
Nomoto, K., Thielemann, F.-K., & Yokoi, K. 1984, ApJ, 286, 664
Pauldrach, A. W. A., Hoffmann, T. L., & Hultzsch, P. J. N. 2014, A&A (arXiv:1307.3067)
Pankey, T. 1962, PhD thesis, Howard Univ.
Perlmutter, S. 1999, ApJ, 517, 565
Phillips, M. M. 1993, ApJL, 413, L105
Riess, A. G., Filippenko, A. V., Challis, P., et al. 1998, AJ, 116, 1009
Roques, J. P., Schanne, S., von Kienlin, A., et al. 2003, A&A, 411, L91
Summa, A., Ulyanov, A., Kromer, M., et al. 2013, A&A, 554, A67
Tajima, H., Blandford, R., Enoto, T., et al. 2010, Proc. SPIE, 7732, 34
Takahashi, T., Abe, K., Endo, M., et al. 2007, PASJ, 59, S35
The, L.-S., Bridgman, W. T., & Clayton, D. D. 1994, ApJS, 93, 531
The, L.-S., Burrows, A., & Bussard, R. W. 1990, ApJ, 352, 731
Vedrenne, G., Roques, J.-P., Schnfelder, V., et al. 2003, A&A, 411, L63
Veigele, M. J. 1973, AD, 5, 51
Woosley, S. E., & Weaver, T. A. 1991, Les Houches, Session LIV, ed. J. Audouze, S. Bludman, R. Mochkovitch, & J. Zinn-Justin (Amsterdam: Elsevier)
Yamaoka, H., Nomoto, K., Shigeyama, T., & Thielemann, F.-K. 1992, ApJL, 393, L55
Zheng, W., Shivvers, I., Filippenko, A. V., et al. 2014, ApJL, 783, L24